Black-Box Impedance Prediction of Grid-Tied VSCs Under Variable Operating Conditions

QI QIU [ID] [1,2,3], **YIFAN HUANG** [1,2], **RUI MA** [ID] [1,2], **JÜRGEN KURTHS** [ID] [4,5,6],
AND MENG ZHAN [ID] [1,2], (Member, IEEE)

[1]School of Electrical and Electronic Engineering, Huazhong University of Science and Technology, Wuhan 430074, China
[2]State Key Laboratory of Advanced Electromagnetic Engineering and Technology, Huazhong University of Science and Technology, Wuhan 430074, China
[3]State Grid Nanchang Electric Power Supply Company, Nanchang 330000, China
[4]Department Complexity Science, Potsdam Institute for Climate Impact Research, 14473 Potsdam, Germany
[5]Institute of Physics, Humboldt University of Berlin, 10099 Berlin, Germany
[6]Institute of Information Technology, Lobachevsky University of Nizhny Novgorod, 603950 Nizhnij Novgorod, Russia

Corresponding author: Meng Zhan (zhanmeng@hust.edu.cn)

ABSTRACT Impedance/admittance models (IM/AMs) have been widely used to analyze the small-signal stability of grid-tied power electronic devices, such as the voltage source converter (VSC). They can be either derived from theoretical analysis under white-box conditions, where all parameters and control structures are fully known, or measured based on experiments under black-box conditions, where the topology and parameters of the controllers are completely unknown. As the IM/AMs depend on specific operating conditions, it is highly desirable to develop fast algorithms for IM/AM prediction (or estimation) under the black-box and variable-operating-point conditions. This article extends the nearly-decoupled AM method for sequence AMs proposed recently by Liu *et al* to fit any unknown control structure, including not only grid-following VSC, but also grid-forming VSC. It is, therefore, referred to as the fully-decoupled IM (FDIM) method. Furthermore, a curve fitting method for the transfer function is proposed to expedite the algorithm, based on the information of a few disturbance frequencies only. Finally, the algorithm is verified by wide simulations and experiments under different situations, including the direct-drive wind turbine generator. The whole approach is expected to be broadly applicable to the stability analysis of power-electronic-based power systems under variable operating conditions.

INDEX TERMS Impedance/admittance prediction, black-box systems, variable operating points, voltage source converter, small-signal stability.

NOMENCLATURE

s	Superscript, the variable in the system dq frame.
c	Superscript, the variable in the controller dq frame.
θ	Phase of the synchronization control part.
$\Delta\theta$	Angle mismatch between the controller and system dq frames.
V_{dc}	Voltage of direct-current bus.
P, P_{in}	Output active power and input active power.
$i_{d,q}$	d- and q-axis components current.
$e_{d,q}$	d- and q-axis components internal potential.
$I_{d,q}$	Steady values of the d- and q-axis components current.
V_d, q	Steady values of the d- and q-axis components voltage.
L_f, R	The filter inductance and resistance of the VSC.
e_{abc}	The potential of the VSC.
V_{tabc}, i_{abc}	The three-phase voltages and currents at the point of common coupling.
V_t, e_t	The voltage amplitude of V_{tabc} and e_{abc}.
$T_{\Delta\theta}$	Coordinate transformation matrix in (1).
$f_{d,qin}, f_{d,qid}$	The intermediate variables in (7).
$f_{d,qvn}, f_{d,qvd}$	The intermediate variables in (7).

f_i, f_v	The intermediate variables in (8).
$f_{d,q\theta}$	The intermediate variables in (8).
g_i, g_v	The intermediate variables in (9).
Z	The impedance matrix, including $Z_{dd}, Z_{dq}, Z_{qd}, Z_{qq}$.
Δ_{gv}	The intermediate variables in (12).
a_{kn}, b_{kn}	The all coefficients in (13).
$\mathbf{x}$	The operating point vector in (15).
$\mathbf{a}_k, \mathbf{b}_k$	The system parameters in (15).
$\mathbf{A}_0, \mathbf{A}_{ij}$	The intermediate variables in (16).
Σ_{1-4}	The intermediate variables in (20).
$\mathbf{m}_{1,2}, \rho_{1,2}$	The intermediate variables in (23).
$\mathbf{M}_1$	The intermediate variables in (27).
p_n, q_n	The intermediate variables in (29).
p, q, k, h	The intermediate variables in (30).
$K_{1,2}, H_{1,2}$	The intermediate variables in (32).
$\mathbf{R}, \mathbf{R}_r$	The intermediate variables in (33) and its real part.
C	The DC capacitance of VSC.
r	The number of opearing points.
Q	Output reactive power.
ω_0	Fundamental frequency of the system.
$k_{p,ip}$	Proportional and integral coefficients of PI controller in the power flow control.
$K_{p,q}$	Gain coefficients of the basic droop control.
$k_{p,iv}$	Proportional and integral coefficient of PI controller in the basic droop control.
$D_{p,q}, J$	Gain coefficient of the virtual synchronous generator control.
N_f	The number of disturbance frequencies in Equ. (36).
Z_{FSIM}	The Impedance calculated by frequency-scan impedanc model in (36).
Z_{FDIM}	The Impedance calculated by fully-decoupled impedanc model in (36).
ε	The relative error of Z_{FSIM} and Z_{FDIM}.
α, β, η_i	The intermediate variables in (43).
k_i	The constants in (43).
$\mathbf{E}_j$	The intermediate variables in (44).

I. INTRODUCTION

Due to increasing pressure of environmental protection and energy resource, a great quantity of solar and wind powers with the form of distributed sources have been connected to grid recently [1], and meanwhile the traditional power system has being gradually transformed into a semiconducting power system (also called power-electronic-based power system) [2]–[5]. As one of most common devices, the voltage source converter (VSC) has been widely used in photovoltaic inverters, wind farms, and high voltage dc transmission system so on. Recently we have been faced with various types of serious stability and oscillation problems in system level caused by power electronic devices, and hence accurate mathematical modeling and analysis of VSC is highly desirable [6]–[8].

Until now there are two major methods for the small-signal stability analysis of power-electronic-based power systems, including the state-space model and the impedance/admittance model (IM/AM) [9]–[11]. The state-space model is a time-domain analytic method based on the system state equation. The state equation is usually established according to the circuit configuration and then linearized on the steady-state operating points. Further the stability of the system can be studied by analyzing the associated Jacobian matrix. But the state-space model is workable only under white-box conditions, in which the system structure and parameters should be fully known. In contrast, generally the IM/AM can be divided into two types. The first is the IM/AM based on theoretical modeling. The transfer function is established according to the system topology to obtain the theoretical IM/AM. Unfortunately, it is also only applicable under white-box conditions. The second is the IM/AM based on measurement. There the IM/AM can be obtained through experiments by frequency sweeping measurement via either series voltage or shunt current injection, under black/gray-box conditions [12]–[15], where usually we cannot get all the structure and parameters of devices for the sake of commercial secrecy. Based on these IM/AM results from either theoretical modeling or measurement, the small-signal stability analysis can be further studied based on the generalized Nyquist stability criterion [16]–[19]. As the black-box or gray-box is more realistic, the IM/AM measurement has been widely used under various practical conditions and has become a dominant method in electric power engineering. In addition, the method of amplitude-phase motion equations has been proposed [20], and the equivalence and relation of all these important methods have been investigated very recently [21], [22].

It is well known that the small-signal stability relies on a linearization around the sufficiently small neighboring of a certain operating point, and the IM/AM of devices should depend on a specific operating point. Even if there is no any change within the power electronic device, any external change would also change the operating point and further the IM/AM result of the device. This makes the IM/AM measurement quite time-consuming under variable operating conditions, especially when we want to exhaustively study the system's stability boundary or fault-set searching for various working conditions. Therefore, it becomes a great challenging to develop proper, fast algorithms for IM/AM prediction (or IM/AM estimation) under both black-box and variable-operating-point conditions.

So far, there is not any work on the IM/AM prediction under fully black-box conditions, to the best knowledge of the authors. Relevant to this target, recently Amin and Molinas proposed a gray-box method to estimate controller parameters based on the already-known control structure [23]. Zhang *et al.* and Gong *et al.* realized admittance estimation based on neural network [24] and multidimensional interpolation [25], respectively. Liu *et al.* proposed a novel "nearly-decoupled AM" (NDAM) model, in which the

sequence-domain AM of VSC by using the phase-locking loop (PLL) synchronization can be obtained under variable operating conditions [26]. The major limitation of the latter method is that it is still a gray-box method, on the assumption that the control structure of VSC should include PLL. Recently, Liu *et al.* [27] further proposed a sequence-domain frequency-coupled impedance model (FCIM) with the corresponding stability criterion, and well studied the problem of subsynchronous oscillation caused by interaction between power electronic equipment and weak AC grids.

This article will extend the NDAM in the sequence domain [26] to the *dq* domain and make some great improvements by applying it to a VSC under an arbitrary control structure and completely black-box conditions. The whole prediction algorithm is, therefore, referred to as fully-decoupled IM (FDIM). It is further improved by a transfer-function curve fitting algorithm. All these are expected to be helpful for system stability analysis and applicable for various practical problems, in particular, when a large number of repetitive IM measurements under variable operating conditions are needed.

The following contents are organized as follows. Section II introduces the detailed algorithm of the fully-decoupled IM. In Section III, a curve fitting method of the transfer function is proposed. In Section IV, the accuracy of our IM prediction under different control strategies is verified by simulations in MATLAB/SIMULINK. Section V is dedicated to validating the FDIM method through hardware-in-the-loop (HIL) experiments of direct-drive wind turbine generators under different operating conditions. Finally, Section VI is devoted to conclusions.

II. FDIM FOR GRID-TIED VSC

A. TYPICAL STRUCTURE OF GRID-TIED VSC

Figure 1(a) schematically shows a grid-tied VSC with an unknown control system under black-box conditions. The symbols L_f and R represent the interfacing inductance and resistance of the VSC, respectively, C denotes the capacitor at the DC side, P_{in} is the input active power at the DC side, e_{abc} is the internal potential of the VSC, and V_{tabc} and i_{abc} are the three-phase voltages and currents at the point of common coupling (PCC). We use V_t and e_t to represent the voltage amplitude of V_{tabc} and e_{abc}, respectively. The PWM is for the pulse width modulation technique. The key objective of the IM method is to study the terminal characteristics of devices, i.e., the linearized relation between the terminal voltages and currents at the PCC, which can be further used for small-signal stability analysis.

The control methods denoted by "control system" in Fig. 1(a) can be diverse. In particular, a typical control structure of the VSC is shown in Fig. 1(b); it includes the vector control based on the Park transformation of the phase-locking loop, which is a typical synchronization technique in renewable energy integration. The outer control loops include the terminal voltage control (TVC) and the DC-link voltage
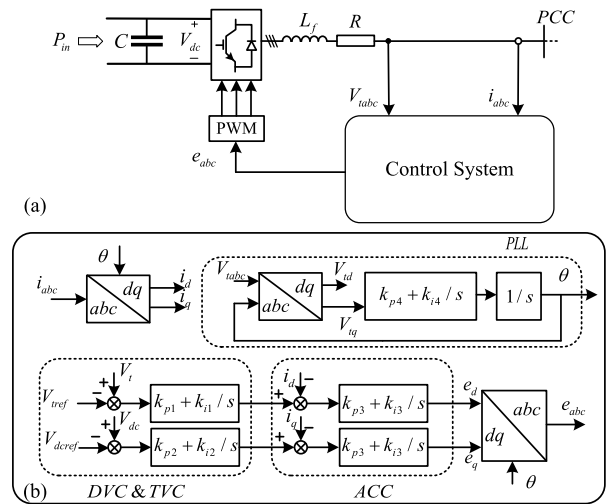

FIGURE 1. (a) Schematic show of general structure for the three-phase grid-tied VSC with its unknown control system under the black-box conditions. (b) Schematic show of typical controllers with the vector control (including TVC and DVC for the outer control loops and ACC for the two inner control loops) and the phase-locking loop for synchronization.
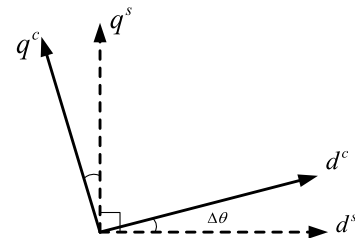

FIGURE 2. Schematic show for the system and controller d-q frames: d^s-q^s and d^c-q^c, respectively. The angle mismatch between the two *dq* frames in dynamical process is denoted by $\Delta\theta$.

control (DVC). The inner control loop is the alternating current control (ACC). θ_{PLL} is the phase output of the PLL. V_{tref} and V_{dcref} are the voltage references, and k_{p1-4} and k_{i1-4} represent the corresponding proportional and integral coefficients of the four PI controllers in the DVC, TVC, ACC, and PLL, respectively.

B. IM OF VSC IN THE DQ DOMAIN

Transformation of the three-phase variables into the *dq* reference frame, namely, from AC signals to DC ones, is an useful technique for the control design of converters. No matter what kind of control system the VSC contains in Fig. 1(a), the inverter system usually has two *dq* frames: one is the system *dq* frame (denoted by d^s-q^s), and the other is the controller *dq* frame (denoted by d^c-q^c); their relation is illustrated in Fig. 2, where the angle mismatch between the two *dq* frames in dynamical process is denoted by $\Delta\theta$. In the steady state, the two coordinates are identical, i.e., $\Delta\theta = 0$. However, if an external disturbance is applied, the two coordinate systems will no longer coincide.

The conversion of the voltage and current vectors in the two coordinate systems is determined by the matrix $T_{\Delta\theta}$,

$$T_{\Delta\theta} = \begin{bmatrix} \cos(\Delta\theta) & \sin(\Delta\theta) \\ -\sin(\Delta\theta) & \cos(\Delta\theta) \end{bmatrix} \quad (1)$$

and

$$\begin{bmatrix} V_d^c \\ V_q^c \end{bmatrix} = T_{\Delta\theta} \begin{bmatrix} V_d^s \\ V_q^s \end{bmatrix}, \quad \begin{bmatrix} I_d^c \\ I_q^c \end{bmatrix} = T_{\Delta\theta} \begin{bmatrix} I_d^s \\ I_q^s \end{bmatrix} \quad (2)$$

where $(V_d^c, V_q^c, I_d^c, I_q^c)$ and $(V_d^s, V_q^s, I_d^s, I_q^s)$ are the steady-state values of (V_d, V_q, I_d, I_q) of the two coordinate systems, respectively. Under the steady-state situation, $\Delta\theta = 0$, $V_d^c = V_d^s = V_d$, $V_q^c = V_q^s = V_q$, $I_d^c = I_d^s = I_d$, and $I_q^c = I_q^s = I_q$, namely,

$$\begin{bmatrix} V_d^c \\ V_q^c \end{bmatrix} = \begin{bmatrix} 1 & 0 \\ 0 & 1 \end{bmatrix} \begin{bmatrix} V_d^s \\ V_q^s \end{bmatrix} \quad (3)$$

Considering a small perturbation $\Delta\theta$ ($\Delta\theta \ll 1$), we have

$$\begin{bmatrix} V_d^c + \Delta V_d^c \\ V_q^c + \Delta V_q^c \end{bmatrix} \approx \begin{bmatrix} 1 & \Delta\theta \\ -\Delta\theta & 1 \end{bmatrix} \begin{bmatrix} V_d^s + \Delta V_d^s \\ V_q^s + \Delta V_q^s \end{bmatrix} \quad (4)$$

or

$$\begin{bmatrix} \Delta V_d^c \\ \Delta V_q^c \end{bmatrix} = \begin{bmatrix} \Delta V_d^s \\ \Delta V_q^s \end{bmatrix} + \Delta\theta \begin{bmatrix} V_q \\ -V_d \end{bmatrix} \quad (5)$$

and, similarly

$$\begin{bmatrix} \Delta I_d^c \\ \Delta I_q^c \end{bmatrix} = \begin{bmatrix} \Delta I_d^s \\ \Delta I_q^s \end{bmatrix} + \Delta\theta \begin{bmatrix} I_q \\ -I_d \end{bmatrix} \quad (6)$$

where the small perturbations of voltage and current at the PCC within the system and the controller dq frames are denoted by $(\Delta V_d^s, \Delta V_q^s, \Delta I_d^s, \Delta I_q^s)$ and $(\Delta V_d^c, \Delta V_q^c, \Delta I_d^c, \Delta I_q^c)$, respectively. Therefore, no matter what kind of control system is used in the VSC, the conversion relation between the small perturbations of the control dq frame and the system dq frame is determined by (5) and (6). The steady-state variables V_d, V_q, I_d and I_q at the PCC can be obtained directly by measurements. Since the dq impedance model in this article is established in the dq coordinate system with the angle of the terminal voltage as the reference angle of the Park transformation, in the steady state, $V_d = V_t$ and $V_q = 0$.

Before developing our black-box impedance model, let us take a closer look at some typical control schemes of the VSC, which have been widely proposed in the literature. Generally we can divide the control structure into two parts, namely the synchronization control part and the other auxiliary control part. Among them, the role of the synchronization control is to generate a reference angle θ in the control system, and the other part is to design a suitable control loop. Generally there are two major divisions for synchronization, namely the grid-following control and the grid-forming control [15], [28]. The grid-following control is to follow the terminal voltage phase angle through the phase-locking loop, as we have seen in Fig. 1(b). In contrast, the grid-forming control provides the phase information mainly based on the active
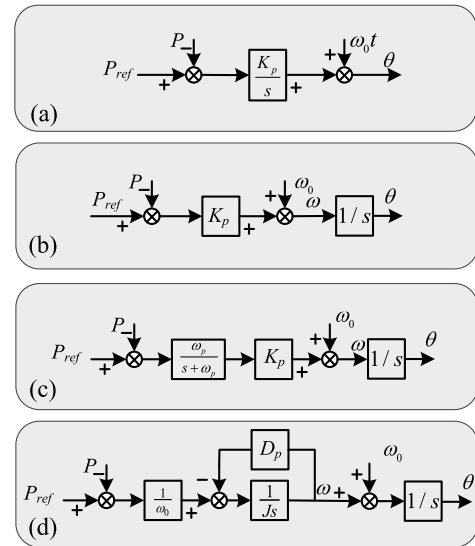

FIGURE 3. Four typical grid-forming control schemes, focusing on their synchronization control parts: (a) PSC, (b) Basic droop control, (c) Droop control with LPFs, and (d) VSG control.

power imbalance between P (active power) and P_{ref} (reference value of active power). For example, four typical control schemes are shown in Figs. 3(a)-(d), including the power-synchronization control (PSC), basic droop control, droop control with low-pass filters (LPFs), and virtual synchronous generator (VSG) control, respectively [29]. We will see that this universality in their control structures could help us to perform IM prediction conveniently.

After performing small-signal derivations on the PLL in Fig. 1(b) and the four different controllers in Fig. 3, we find that $\Delta\theta$ can always be written in a unified form,

$$\Delta\theta = \begin{bmatrix} f_{din} & f_{qin} \\ f_{did} & f_{qid} \end{bmatrix} \begin{bmatrix} \Delta I_d^s \\ \Delta I_q^s \end{bmatrix} + \begin{bmatrix} f_{dvn} & f_{qvn} \\ f_{dvd} & f_{qvd} \end{bmatrix} \times \begin{bmatrix} \Delta V_d^s \\ \Delta V_q^s \end{bmatrix} \quad (7)$$

These eight variables including $f_{din}, f_{did}, f_{qin}, f_{qid}, f_{dvn}, f_{dvd}, f_{qvn},$ and f_{qvd} are intermediate variables generated by linearization. They are all implicit functions of the operating points, that is, the implicit function formula does not change with the change of the operating points. For the detailed derivations, see Appendix A. As usually $V_d = V_t$ and $V_q = 0$, only three variables of the operating points: $V_t, I_d,$ and I_q are needed.

We emphasize that only based on these general relations, can we get deeply into the internal structure of impedance for any black-box controlled VSC. Although we cannot exhaustively study all existing different control schemes in the literature, the above relation is expected to be generally applicable. It is also worth noting that although under the VSG control in Fig. 3(d), the output angle θ is the internal voltage angle of the VSC (e_t) instead of the terminal voltage angle at the

PCC (V_t), $\Delta\theta$ still represents the angle mismatch between the system and the controller dq frames in the dynamical process, and does not affect our impedance modeling.

For the PLL synchronization control, the theoretical impedance expression of VSC in the dq domain has already been deduced in Refs. [16] and [18]. After linearizing the controllers, all the intermediate variables except $\Delta\theta$ are a linear function of the operating points. Namely,

$$\begin{bmatrix} f_{i1} & f_{i2} \\ f_{i3} & f_{i4} \end{bmatrix} \begin{bmatrix} -\Delta I_d^s \\ -\Delta I_q^s \end{bmatrix} = \begin{bmatrix} f_{v1} & f_{v2} \\ f_{v3} & f_{v4} \end{bmatrix} \begin{bmatrix} \Delta V_d^s \\ \Delta V_q^s \end{bmatrix}$$
$$+ \Delta\theta \begin{bmatrix} f_{d\theta} \\ f_{q\theta} \end{bmatrix} \quad (8)$$

where all $f_{i1-4}, f_{v1-4}, f_{d\theta}$, and $f_{q\theta}$ have a linear relation with the operating points (V_t, I_d, and I_q). Again this relation in (8) is believed as workable for any general black-box VSC.

Substituting (7) into (8), we obtain

$$\begin{bmatrix} g_{i1} & g_{i2} \\ g_{i3} & g_{i4} \end{bmatrix} \begin{bmatrix} -\Delta I_d^s \\ -\Delta I_q^s \end{bmatrix} = \begin{bmatrix} g_{v1} & g_{v2} \\ g_{v3} & g_{v4} \end{bmatrix} \begin{bmatrix} \Delta V_d^s \\ \Delta V_q^s \end{bmatrix} \quad (9)$$

where

$$\begin{cases} g_{i1} = (f_{i1}f_{did} + f_{d\theta}f_{din})f_{qid}f_{dvd}f_{qvd} \\ g_{i2} = (f_{i2}f_{qid} + f_{d\theta}f_{qin})f_{did}f_{dvd}f_{qvd} \\ g_{i3} = (f_{i3}f_{did} + f_{q\theta}f_{din})f_{qid}f_{dvd}f_{qvd} \\ g_{i4} = (f_{i4}f_{qid} + f_{q\theta}f_{qin})f_{did}f_{dvd}f_{qvd} \\ g_{v1} = (f_{v1}f_{dvd} + f_{d\theta}f_{dvn})f_{did}f_{qid}f_{qvd} \\ g_{v2} = (f_{v2}f_{qvd} + f_{d\theta}f_{qvn})f_{did}f_{qid}f_{dvd} \\ g_{v3} = (f_{v3}f_{dvd} + f_{q\theta}f_{dvn})f_{did}f_{qid}f_{qvd} \\ g_{v4} = (f_{v4}f_{qvd} + f_{q\theta}f_{qvn})f_{did}f_{qid}f_{dvd} \end{cases} \quad (10)$$

Based on these equations, one can find that all g_{i1-4} and g_{v1-4} have a polynomial, nonlinear relation with the operating points.

Hence according to the impedance definition of the VSC,

$$\begin{bmatrix} \Delta V_d^s \\ \Delta V_q^s \end{bmatrix} = \begin{bmatrix} Z_{dd} & Z_{dq} \\ Z_{qd} & Z_{qq} \end{bmatrix} \begin{bmatrix} -\Delta I_d^s \\ -\Delta I_q^s \end{bmatrix} \quad (11)$$

we can explicitly express each element of the impedance matrix Z as

$$\begin{cases} Z_{dd} = (g_{i1}g_{v4} - g_{v2}g_{i3})\Delta_{gv}^{-1} \\ Z_{dq} = (g_{i2}g_{v4} - g_{v2}g_{i4})\Delta_{gv}^{-1} \\ Z_{qd} = (g_{i3}g_{v1} - g_{v3}g_{i1})\Delta_{gv}^{-1} \\ Z_{qq} = (g_{i4}g_{v1} - g_{v3}g_{i2})\Delta_{gv}^{-1} \end{cases} \quad (12)$$

where $\Delta_{gv} = g_{v1}g_{v4} - g_{v2}g_{v3}$.

C. DECOMPOSITION OF IM IN THE FDIM

Based on the above theoretical analysis, one can find that the four elements of the IM in (12) are complicated nonlinear

functions of system parameters, operating points, and disturbance frequency ω (as $s = j\omega$). In contrast, all f's in (7) and (8) are linear functions of the operating points, and all g_{i1-4} and g_{v1-4} in (10) are their polynomial functions. Based on these observations, as the first step, we like to reshape the IM in (12) by decoupling the operating points.

As g_{i1-4} and g_{v1-4} can be written as polynomials of the operating points (I_d, I_q, and V_t), including one constant term, three first-order terms (I_d, I_q, and V_t), six second-order terms ($I_d^2, I_q^2, V_t^2, I_dI_q, I_dV_t$, and I_qV_t), and many third-order terms ($I_d^3, I_q^3, V_t^3, I_d^2I_q, \ldots$), etc., and importantly in the per-unit system, $I_d \leq 1, I_q \leq 1$, and $V_t \leq 1$, which indicates that the lower-order terms should have more contribution. Then g_{i1-4} and g_{v1-4} can be written as

$$\begin{cases} g_{ik} = a_{k1} + a_{k2}I_d + a_{k3}I_q + a_{k4}V_t + a_{k5}I_d^2 + a_{k6}I_q^2 + \cdots \\ g_{vk} = b_{k1} + b_{k2}I_d + b_{k3}I_q + b_{k4}V_t + b_{k5}I_d^2 + b_{k6}I_q^2 + \cdots \end{cases} \quad (13)$$

based on their different orders, where all coefficients a_{kn} and b_{kn} for $k = 1, 2, 3, 4$ and $n = 1, 2, 3, 4, \ldots$ depend on the system parameters and disturbance frequency only, and they are irrelevant with the operating-point information.

Equations (13) can be rewritten in the compact vector forms:

$$\begin{cases} g_{ik} = a_k^T x \\ g_{vk} = b_k^T x, \quad k = 1, 2, 3, 4 \end{cases} \quad (14)$$

and

$$\begin{cases} x = \begin{bmatrix} 1 & I_d & I_q & V_t & I_d^2 & I_q^2 & I_dI_q & \cdots \end{bmatrix}^T \\ a_k = \begin{bmatrix} a_{k1} & a_{k2} & a_{k3} & a_{k4} & \cdots \end{bmatrix}^T \\ b_k = \begin{bmatrix} b_{k1} & b_{k2} & b_{k3} & b_{k4} & \cdots \end{bmatrix}^T \end{cases} \quad (15)$$

where a_k and b_k denote the induced system parameters. They contain the combined information of the system parameters and disturbance frequency, and x represents the operating point vector separately. Clearly now the operating-point information has been completely decoupled.

Further substituting (14) and (15) into (12) gives

$$\begin{cases} Z_{dd} = x^T A_{11} x (x^T A_0 x)^{-1} \\ Z_{dq} = x^T A_{12} x (x^T A_0 x)^{-1} \\ Z_{qd} = x^T A_{21} x (x^T A_0 x)^{-1} \\ Z_{qq} = x^T A_{22} x (x^T A_0 x)^{-1} \end{cases} \quad (16)$$

with the matrices A_0 and A_{ij} (for $i, j = 1, 2$) expressed by

$$\begin{cases} A_0 = b_1 b_4^T - b_2 b_3^T \\ A_{11} = a_1 b_4^T - a_3 b_2^T, \quad A_{12} = a_2 b_4^T - a_4 b_2^T \\ A_{21} = a_3 b_1^T - a_1 b_3^T, \quad A_{22} = a_4 b_1^T - a_2 b_3^T \end{cases} \quad (17)$$

Hence the four IM elements (Z_{dd}, Z_{dq}, Z_{qd}, and Z_{qq}) in (16) have been explicitly divided into the operating point vector

x, and the matrices A_0 and A_{ij} (for i, $j = 1$, 2), which depend on the induced device parameters a_{1-4} and b_{1-4} only. Now the operating point in the IM prediction has been fully decoupled, and this point is believed as a great improvement, in comparison to the NDAM method in [26]. Based on (16), we can get IM for any operating condition immediately, under the condition that we have obtained all the induced system parameters of the device, a_k and b_k, which should be further achieved by parameter identification from multiple IM measurements.

D. IDENTIFICATION METHOD IN THE FDIM

For the aim of parameter identification of all induced system parameters (a_k and b_k), first we should obtain their possible restriction conditions, based on the already-known information of the operating point vector x and the IM from several IM measurements. Inputting (14) into (9), we have the following homogeneous equations

$$\begin{cases} g_{i1}\Delta I_d^s + g_{i2}\Delta I_q^s + g_{v1}\Delta V_d^s + g_{v2}\Delta V_q^s = 0 \\ g_{i3}\Delta I_d^s + g_{i4}\Delta I_q^s + g_{v3}\Delta V_d^s + g_{v4}\Delta V_q^s = 0 \end{cases} \quad (18)$$

According to the definition of the dq-domain impedance in (11), we have

$$\begin{cases} \Delta V_d^s = -(Z_{dd}\Delta I_d^s + Z_{dq}\Delta I_q^s) \\ \Delta V_q^s = -(Z_{qd}\Delta I_d^s + Z_{qq}\Delta I_q^s) \end{cases} \quad (19)$$

Substituting (19) into (18) gives

$$\begin{cases} \Sigma_1 \Delta I_d^s + \Sigma_2 \Delta I_q^s = 0 \\ \Sigma_3 \Delta I_d^s + \Sigma_4 \Delta I_q^s = 0 \end{cases} \quad (20)$$

where

$$\begin{cases} \Sigma_1 = -Z_{dd}g_{v1} - Z_{qd}g_{v2} + g_{i1} \\ \Sigma_2 = -Z_{dq}g_{v1} - Z_{qq}g_{v2} + g_{i2} \\ \Sigma_3 = -Z_{dd}g_{v3} - Z_{qd}g_{v4} + g_{i3} \\ \Sigma_4 = -Z_{dq}g_{v3} - Z_{qq}g_{v4} + g_{i4} \end{cases} \quad (21)$$

Since both ΔI_d^s and ΔI_q^s represent external disturbances in the small-signal perturbation tests, they should be independent. Thus the relations in (20) hold true only if their coefficients Σ_{1-4} are all zero, i.e., $\Sigma_{1-4} = 0$. Then inputting (14) into (21) gives

$$\begin{cases} -Z_{dd}b_1^T x - Z_{qd}b_2^T x + a_1^T x = 0 \\ -Z_{dq}b_1^T x - Z_{qq}b_2^T x + a_2^T x = 0 \\ -Z_{dd}b_3^T x - Z_{qd}b_4^T x + a_3^T x = 0 \\ -Z_{dq}b_3^T x - Z_{qq}b_4^T x + a_4^T x = 0 \end{cases} \quad (22)$$

Now we have obtained the restricted relations between the impedances (Z_{dd}, Z_{dq}, Z_{qd}, and Z_{qq}), the operating point vectors x, and the system parameters (a_k and b_k). These equations in (22) would become the basis for the parameter identification of a_k and b_k.

Before doing this, we like to express Eqs. (22) in a more compact form. Taking the first and third ones in Eqs. (22) into one group, and the second and forth ones into the other group, we have

$$\begin{cases} m_1^T \boldsymbol{\rho}_1 = 0 \\ m_1^T \boldsymbol{\rho}_2 = 0 \end{cases} \quad (23)$$

and

$$\begin{cases} x^T a_2 = m_2^T \begin{bmatrix} b_1^T & b_2^T \end{bmatrix}^T \\ x^T a_4 = m_2^T \begin{bmatrix} b_3^T & b_4^T \end{bmatrix}^T \end{cases} \quad (24)$$

respectively, where

$$\begin{cases} m_1 = \begin{bmatrix} -Z_{dd}x^T & -Z_{qd}x^T & x^T \end{bmatrix}^T \\ \boldsymbol{\rho}_1 = \begin{bmatrix} b_1^T & b_2^T & a_1^T \end{bmatrix}^T \\ \boldsymbol{\rho}_2 = \begin{bmatrix} b_3^T & b_4^T & a_3^T \end{bmatrix}^T \\ m_2 = \begin{bmatrix} Z_{dq}x^T & Z_{qq}x^T \end{bmatrix}^T \end{cases} \quad (25)$$

Observing Eqs. (23) and (25), one can see that ρ_1 and ρ_2 are the two solutions of the same linear equation $m_1^T \rho = 0$. After solving (23), we can obtain a_1, a_3, and b_{1-4}. Similarly, we can further solve (24) and obtain a_2 and a_4. Therefore, in principle we can obtain all these necessary parameters a_{1-4} and b_{1-4}, and accomplish the IM prediction in (16).

E. DETAILED ALGORITHM OF THE FDIM

The detailed algorithm of the FDIM is listed as follows.

i) Since the system control topology and system parameters are all unknown, and the real combination of the operating points (I_d, I_q, V_t) in x is undecided under the black-box conditions, we first need to fix the form of x, which usually starts from a constant term, first-order terms (I_d, I_q, and V_t), and second-order terms ($I_d^2, I_q^2, V_t^2, I_d I_q, I_d V_t$, and $I_q V_t$), based on the fact that lower-order terms usually have a stronger impact, i.e.,

$$x = \begin{bmatrix} 1 & I_d & I_q & V_t & I_d^2 & I_q^2 & V_t^2 & I_d I_q & I_d V_t & I_q V_t \end{bmatrix}^T \quad (26)$$

clearly the size of x is 10×1, the same as that of a_{1-4} and b_{1-4}.

ii) Suppose that the dq-domain impedance elements (Z_{dd}, Z_{dq}, Z_{qd}, and Z_{qq}), the terminal currents (I_d and I_q), and the terminal voltage (V_t) of different operating points have been already obtained by N perturbation tests in the impedance measurements. Substituting them into (23) and (24), we get the following linear algebraic equations:

$$M_1 \rho = 0 \quad (27)$$

and

$$\begin{cases} X^T a_2 = M_2^T \begin{bmatrix} b_1^T & b_2^T \end{bmatrix}^T \\ X^T a_4 = M_2^T \begin{bmatrix} b_3^T & b_4^T \end{bmatrix}^T \end{cases} \quad (28)$$

where $M_1 = [m_{11}, m_{12}, \ldots, m_{1N}]^T$ and its size is $N \times 30$; $X = [x_1, x_2, \ldots, x_N]^T$ and its size is $N \times 10$; $M_2 = [m_{21}, m_{22}, \ldots, m_{2N}]^T$ and its size is $N \times 20$; and the vector ρ is the set of all the solutions of (27), representing either ρ_1 or ρ_2, and the size of the vector ρ is 30×1.

iii) Next we solve the homogeneous linear equations (27). Obviously, ρ_1 and ρ_2 are linearly independent, which means that the dimension of the vector space of solutions of (27) is at least 2. In view of this, the rank of M_1 must be no more than 28 ($30 - 2 = 28$). Furthermore, the vector space of solutions of (27), i.e., ρ_1 and ρ_2 can be obtained only if the rank of M_1 reaches the maximum, and the total number of perturbation experiments, N, should be large enough. For convenience, we choose $N = 28$ different groups of operating points accompanying with their corresponding impedance matrices from the IM measurement. Hence we obtain b_{1-4}, a_1, and a_3 from (27), and then substitute them into (28) to get a_2 and a_4.

iv) Finally, based on these identified induced system parameters of a_{1-4} and b_{1-4}, we can easily calculate the IM in (16), for any varying operating point.

It is worth noting that since the assumed composition of x in (26) may be too sufficient, the addition of more terms would add more new free variables to the solution vectors $\boldsymbol{\rho}$. Then the number of the basic solution set of (27) may be more than two. In fact, under certain preconditions, any two linearly independent solutions of (27) are equivalent to the model parameter vectors $\boldsymbol{\rho}_1$ and $\boldsymbol{\rho}_2$ in calculating the FDIM. For the detailed proof and precondition, see Appendix B. If the precondition is not met, it means that the selection of the operating points are inappropriate, and the known operating points and their corresponding impedances need to be increased. If the basic solution set of (27) is less than two, it means that the assumed element of x is insufficient. Then we need to increase the combination of operating points in x in (26), such as the third-order terms (including I_d^3, I_q^3, V_t^3, $I_d^2 I_q$, ...). However, in all the studied cases in the paper, this does not happen.

In addition, in order to ensure the accuracy of the FDIM, any two sets of operating points used for the parameter identification should be significantly different from each other, and the operating points near operating boundary should be selected as possible as we can.

III. FURTHER IMPROVEMENT: CURVE-FITTING BASED FDIM

Basically, we have already accomplished the IM prediction by applying the above algorithm on any fixed disturbance frequency and step by step on any frequency region which we are interested in; this manner is similar to the impedance measurement by frequency sweeping. Actually, we can also realize this in a more efficient manner by using a transfer function curve fitting technique. Namely we can estimate the IM within the whole frequency region, once and for all, based on several already-known IM data under certain frequencies

only, if we can predict the specific transfer function curve form. For a comparison, we call the former method as point-by-point FDIM, whereas the latter one as curve-fitting based FDIM.

Below let us introduce the curve-fitting based FDIM in detail. First, we assume that the highest power of s in the numerator and denominator of the transfer function is n, and write the transfer function as

$$f_{(s)} = \frac{p_0 + p_1 s + \cdots + p_n s^n}{q_0 + q_1 s + \cdots + q_n s^n} \tag{29}$$

where both $p_n \neq 0$ and $q_n \neq 0$ are not allowed.

Express (29) in the form of the homogeneous linear equation:

$$k^T p = h^T q \tag{30}$$

where

$$\begin{cases} p = [p_0 \ p_1 \ \cdots \ p_n]^T \\ q = [q_0 \ q_1 \ \cdots \ q_n]^T \\ k = [1 \ s \ \cdots \ s^n]^T \\ h = [f_{(s)} \ f_{(s)} s \ \cdots \ f_{(s)} s^n]^T \end{cases} \tag{31}$$

Then suppose that we have S group data of amplitude frequency response under different disturbance frequency ω's, namely, s ($s = j\omega$) and $f_{(s)}$ in (30) are different for different ω's. Since there are $2n + 2$ unknown parameters: p_{0-n}, q_{0-n} in (30), we may choose $S = 2n + 2$ to have the square matrix forms of K_1, K_2, H_1, and H_2, and obtain

$$\begin{cases} K_1 p = H_1 q \\ K_2 p = H_2 q \end{cases} \tag{32}$$

where the specific expressions of K_1, K_2, H_1, and H_2 are presented in detail in Appendix C.

Since K_1 is a Vandermonde matrix and the selected s's in K_1 are independent, the determinant of K_1 is not equal to 0 and hence K_1 is invertible. Similarly, K_2, H_1, and H_2 are all invertible.

Rearranging (32), we have

$$Rq = q \tag{33}$$

where

$$R = H_2^{-1} K_2 K_1^{-1} H_1 \tag{34}$$

Here R is a complex matrix. Denote R_r as the real part and R_i the imaginary part of R. As q is a real vector, we obtain

$$R_r q = q \tag{35}$$

Therefore, q can be obtained by calculating the eigenvector corresponding to R_r with an eigenvalue of 1. Furthermore, p can be solved in any equation in (32), and hence the parameters p and q in the transfer function in (29) can be fully obtained. It should be noted that in the calculation, as we do not know the specific form of the transfer function, we usually

start from $n = 1$, increase n gradually, and stop the calculation until the eigenvector corresponding to the eigenvalue 1 of R_r in (35) is unique.

Wide numerical simulation results have shown that the curve-fitting based FDIM can indeed greatly improve the calculation efficiency, as it deals with the estimation of the transfer function in a global manner. In contrast, the point-by-point FDIM costs longer calculation time. Compared to the classical frequency-domain transfer function curve fitting, which is usually approximated by a rational function of factorizing numerator and denominator; see, e.g., [30] and [31], our curve-fitting based FDIM method is superb, when the order of the transfer function is low.

IV. SIMULATION AND VERIFICATION

A. SYSTEM CONFIGURATION

Without losing generality, the system parameters in Fig. 1(a) for a grid-tied VSC with an unknown control system are chosen as follows: $C = 98\ mF$, $R = 0.1\Omega$, $L_f = 75.77\mu F$, and $U_{dc} = 1400V$. The base values of the PCC bus voltage and power are 690 V and 2 MVA, respectively.

To test the FDIM algorithm, we have studied several major control forms, such as the PLL combined with ACC, DVC, and TVC, the PLL combined with ACC and power flow control, the droop control, the virtual synchronous generators control, etc., as shown in Figs. 1 and 3. For the black-box study, we do not know any information about the system parameter and the control forms in advance. The whole system is established and simulated in MATLAB/SIMULINK. Totally 28 sets of operating points are necessary for the parameter identification and the last operating point (set $r = 29$ in the bottom row) is used for verification; they are all listed in Table 1. It is worth noting that in the simulations, the information of any operating point of V_t, P ($P = V_t I_d$), and Q ($Q = -V_t I_q$) is recorded instead of that of I_d, I_q, and V_t, based on the convention of electric power engineering. As $V_d = V_t$ and $V_q = 0$, only three variables are independent and both (V_t, P, Q) and (I_d, I_q, V_t) can be used.

B. PREDICTION OF IM UNDER THE ACC, DVC, TVC, AND PLL

The control strategies of the ACC, DVC, TVC, and PLL are adopted, as shown in Fig. 1(b). Without losing generality, the system parameters are chosen as: $k_{p1} = 3.5$, $k_{i1} = 140$, $k_{p2} = 1$, $k_{i2} = 100$, $k_{p3} = 0.3$, $k_{i3} = 160$, $k_{p4} = 50$, and $k_{i4} = 2000$.

First, the IM of the VSC under 28 sets of different operating points are obtained by the frequency-scan perturbation tests, the same as the usual IM measurement. These data serve as our basis for the parameter identification of a_{1-4} and b_{1-4}. The perturbation frequencies f_{set} are obtained by randomly selecting from 1 Hz to 1000 Hz. Second, the induced parameters, a_{1-4} and b_{1-4}, at each disturbance frequency are identified, as described in Section II. Then by using the point-by-point FDIM, the impedance of each disturbance frequency under the operating point of the 29th set ($r = 29$ in

TABLE 1. Operating points used to identification ($r = 1 - 28$) and verification ($r = 29$).

Set r	V_t (pu)	P (pu)	Q (pu)	Set r	V_t (pu)	P (pu)	Q (pu)
1	0.9704	0.8219	0.6769	15	0.8828	0.7020	0.5528
2	0.9657	0.6050	0.7701	16	0.7449	0.3319	-0.2180
3	0.6392	0.3496	-0.5849	17	0.8547	0.6450	0.3829
4	0.9824	0.1548	-0.9247	18	0.8399	0.5502	0.5667
5	0.9786	0.4750	-0.5887	19	0.5595	0.2788	-0.5145
6	0.5709	0.2408	-0.4747	20	0.6702	0.3922	0.3702
7	0.8961	0.8598	-0.2791	21	0.8756	0.2234	-0.0104
8	0.5179	0.4397	-0.4495	22	0.8495	0.7569	-0.7804
9	0.8394	0.6360	-0.4082	23	0.7736	0.1072	0.5426
10	0.6961	0.4563	0.4578	24	0.6288	0.5286	0.3090
11	0.8530	0.0272	0.3806	25	0.9071	0.2209	-0.7788
12	0.5231	0.0508	-0.3384	26	0.6750	0.1327	0.3360
13	0.8474	0.2687	-0.7630	27	0.8080	0.3824	0.2397
14	0.5172	0.2269	0.1225	28	0.9154	0.5358	-0.0910
29	**1.0000**	**0.8000**	**0.0160**	-	-	-	-

Table 1) is obtained. Finally, by using a faster curve-fitting based FDIM, the IM under the operating point of the 29th set can be predicted, as described in Section III. To clearly exhibit the whole calculation process, a detailed flow chart of the curve-fitting based FDIM prediction method is given in Appendix D.

In simulations, we found that the running time of the FDIM depends on the time consumed by impedance measurement. If the test operating point is selected properly, for a single frequency point, the running time of the FDIM is the time of 28 groups of impedance measurements.

As one typical example, the results of the frequency-scan IM (FSIM) (solid line), point-by-point FDIM (cross points), and curve-fitting based FDIM (dashed line) are compared in Fig. 4, where clearly both estimations from the point-by-point based FDIM and the curve-fitting based FDIM fit with the FSIM from measurement almost perfectly. This figure well verifies the accuracy of the FDIM. Note that due to space constraints, only the result of Z_{dq} is presented here and all other elements show similar excellent results.

C. PREDICTION OF IM UNDER THE ACC, PFC, AND PLL

The control strategy is now changed to the ACC, PFC, and PLL, as shown in Fig. 5. Without losing generality, the system parameters are $k_{pp} = 0.0028$, $k_{ip} = 7$, $k_{p3} = 0.3$, $k_{i3} = 160$, $k_{p4} = 50$, and $k_{i4} = 2000$ [18].

The procedure to compute the FDIM is the same, and the amplitude and phase response results by using the frequency-scan IM, point-by-point FDIM, and curve-fitting based FDIM are presented in Fig. 6. Again we see that the IM prediction results match with the IM measurement result well.
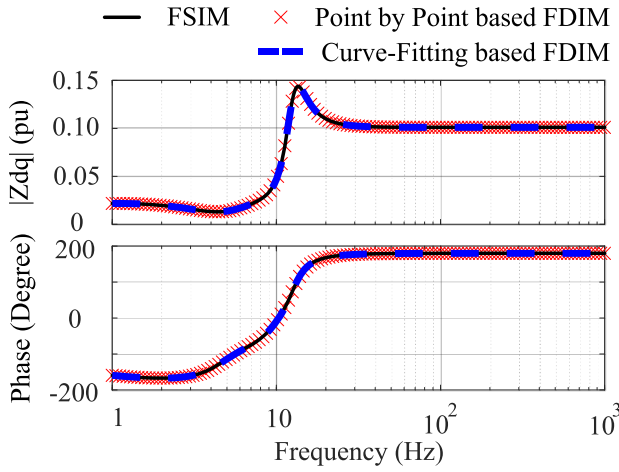
FIGURE 4. Amplitude and phase responses of the impedance element Z_{dq} under the ACC, DVC, TVC, and PLL, for comparing the results of the IM measurement (FSIM) and the IM predictions (point-by-point based FDIM and curve-fitting based FDIM).
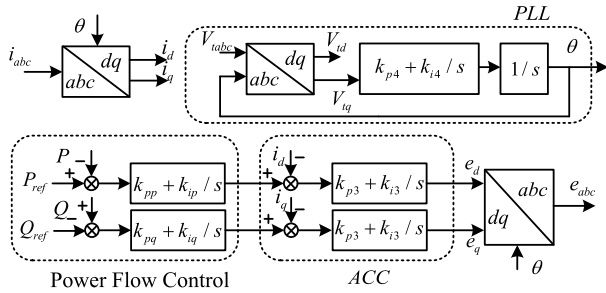

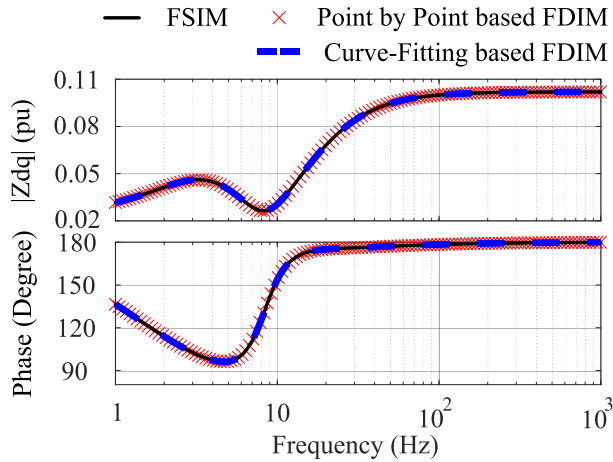**FIGURE 5.** Control strategy of the ACC, PFC, and PLL.

FIGURE 6. Amplitude and phase responses of the impedance element Z_{dq} under the ACC, PFC, and PLL.

D. PREDICTION OF IM UNDER THE BASIC DROOP CONTROL

In this section, the basic droop control is adopted, as shown in Fig. 7. Since the small-signal output angle $\Delta\theta$'s of the PSC,
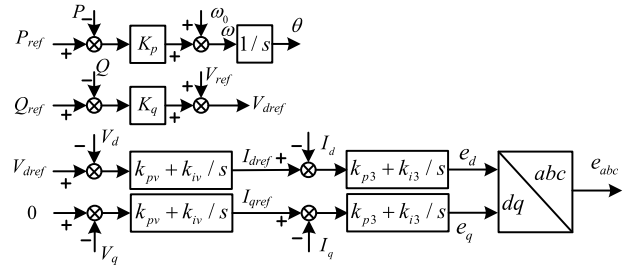

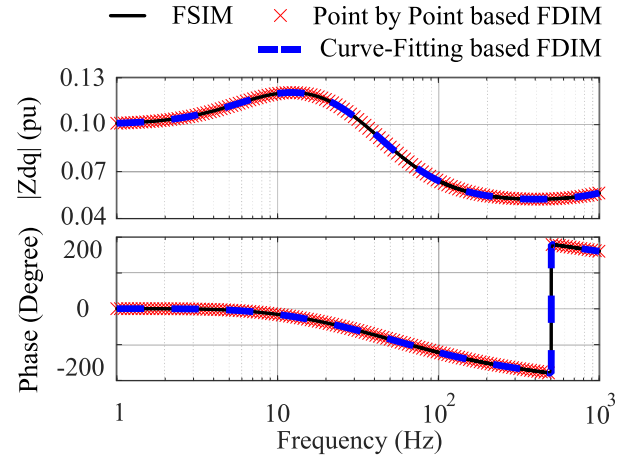**FIGURE 7.** Control strategy of the basic droop control.

FIGURE 8. Amplitude and phase responses of the impedance element Z_{dq} under the basic droop control.

the basic droop control, and the droop control with LPFs in Figs. 3(a)-(c) are similar (see Appendix A), here we only take the basic droop control as an example. Without losing generality, we choose the following system parameters: $k_p = 0.02$, $k_q = 0.1$, $k_{pv} = 0.6$, $k_{iv} = 700$, $k_{p3} = 0.4$, $k_{i3} = 15$, and $\omega_0 = 2\pi \times 50$ [32], [33]. The amplitude and phase response comparison results are presented in Fig. 8. Clearly although there is a jump at around 500 Hz in its phase response curve, their matching is still good.

E. PREDICTION OF IM UNDER THE VSG CONTROL

We have also tested our FDIM prediction algorithm by using the virtual synchronous generator control [34], shown in Fig. 9. VSG is a control scheme applied to inverters of distributed power generation units by imitating the behavior of a synchronous generator. Without losing generality, the following system parameters are chosen: $D_p = 10$, $D_q = 1/15$, $J = 0.5$, and $\omega_0 = 2\pi \times 50$ [35], [36]. The final comparison results are shown in Fig. 10. Again they match well.

V. EXPERIMENTAL RESULTS
A. TEST SYSTEM CONFIGURATION

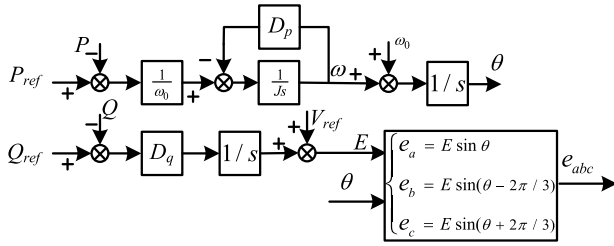In order to further verify the accuracy of the FDIM method, we apply the algorithm to a larger power system consisting
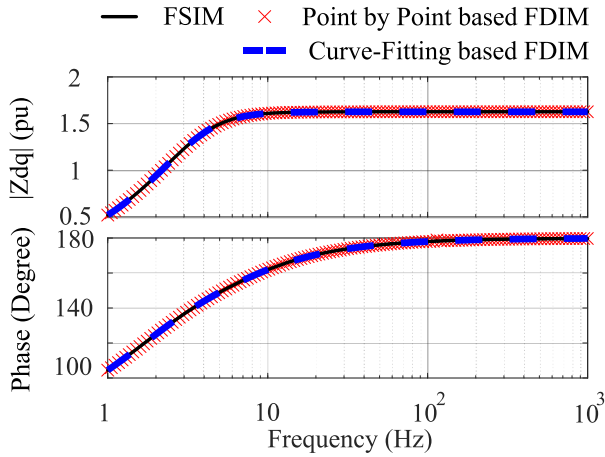
FIGURE 9. Control strategy of the VSG control.

FIGURE 10. Amplitude and phase responses of the impedance element Z_{dq} under the VSG control.

TABLE 2. Parameters of the test system.

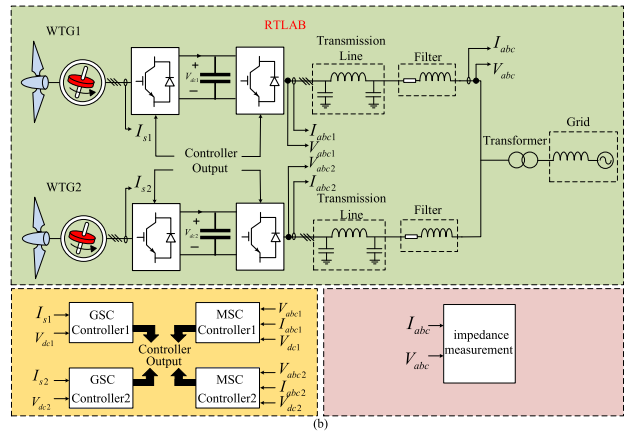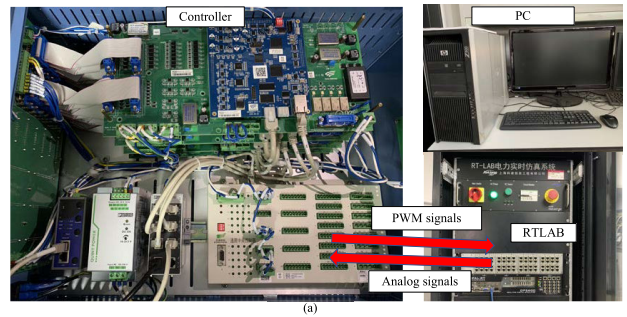| Symbol	Description	Value
S_{base}	Base value of power	1MW
V_{base}	Base value of voltage	690V
f_{base}	Base value of frequency	50Hz
C	DC side capacitor	0.1F
C_{line}	Equivalent capacitance of transmission line	1.25μF
L_{line}	Equivalent inductance of transmission line	0.32mH
L_f	Inductance of filter	1mH
R	Resistance of filter	0.1Ω
K	Transformer ratio	690/35000
L_g	Inductance of grid	0.69mH

FIGURE 11. Photographs of the experimental setup (a) and its schematic diagram (b).

of direct-drive wind turbine generators (WTGs). Different with the previous tests in the article, here we consider the case of non-constant active power on the DC-link capacitor, which is more reasonable in practical scenarios. We carry out hardware-in-the-loop (HIL) experiments based on the RTLAB. The digital signal processing (DSP) used is a WTG simulation produced by GoldWind company. In the experiments, the RTLAB simulates the dynamics of power electronics and other electromagnetic components, and outputs analog signal to the DSP control system to realize the control algorithm and modulation, and then the DSP feedbacks the PWM pulse signal to the RTLAB. In addition, because the controller is an integrated dual-WTG controller, the operating point of the second WTG (WTG2) should be consistent with that of the first WTG (WTG1) and the test is only on the WTG1 to verify the accuracy of the fully decoupled impedance model.

The whole experimental platform and the schematic diagram are illustrated in Fig. 11. Without losing generality, the system parameters are all listed in Table 2.

B. PREDICTION RESULTS OF THE FDIM

The procedure to compute the FDIM is completely consistent with the above simulation. Due to the voltage amplitude and power limitation in the experimental setup, again 28 sets of operating points for identification were re-selected in the

experiment, as shown in Table 3. In order to verify the accuracy of FDIM, three sets of operating points, shown in Table 4, are arbitrarily chosen and used for the test. Since we do not know the internal structure of the controller, we treat it as a black box. Therefore, we like to verify whether the predicted impedance at the given operating points is consistent with the measured impedance. The normalized error ε is defined as

$$\varepsilon = \frac{1}{4N_f} \sum_{N_f} \sum_{i,j=1}^{2} \frac{|Z_{ij,FDIM} - Z_{ij,FSIM}|}{|Z_{ij,FSIM}|} \quad (36)$$

TABLE 3. Operating points used to identification in the experiment.

Set r	V_t (pu)	P (pu)	Q (pu)	Set r	V_t (pu)	P (pu)	Q (pu)
1	1.0177	0.7790	0.2001	15	0.9410	0.6863	0.1602
2	0.9678	0.5984	0.2650	16	0.8469	0.3030	-0.1040
3	0.8420	0.2867	-0.2534	17	0.8568	0.6288	0.1217
4	0.9850	0.1397	-0.9356	18	0.8421	0.0119	-0.0005
5	0.9808	0.4603	-0.9514	19	0.9458	0.4289	-0.7672
6	0.9757	0.2005	-0.7911	20	0.8723	0.3889	0.1716
7	0.8984	0.8187	-0.6861	21	0.9780	0.2151	-0.1981
8	0.9201	0.6145	-0.7737	22	0.8514	0.6756	-0.3470
9	0.9416	0.4318	-0.7673	23	0.9762	0.3919	-0.8755
10	0.9986	0.4521	0.2602	24	0.9312	0.5176	0.0849
11	0.9554	0.2754	0.2397	25	0.9152	0.1963	-0.9736
12	0.9253	0.1911	-0.5600	26	0.9674	0.2802	0.1694
13	0.9486	0.2586	-0.9919	27	0.9101	0.3730	0.0523
14	0.9149	0.2174	-0.0330	28	0.9186	0.5247	-0.3757

TABLE 4. Operating points for verification.

Set r	V_t (pu)	P (pu)	Q (pu)	ε (%)
1	1.0021	0.7729	-0.3512	4.25
2	0.9980	0.8202	-0.0800	2.88
3	0.9181	0.3872	-0.7923	1.45

FIGURE 12. Comparison of the amplitude and phase responses of the four impedance elements of the WTG1 for set 1 in Table 4.

where N_f is the number of disturbance frequencies and the final ε values are given in Table 4. We find that the error between the predicted FDIM and the measured FSIM is small; $\varepsilon < 5\%$.

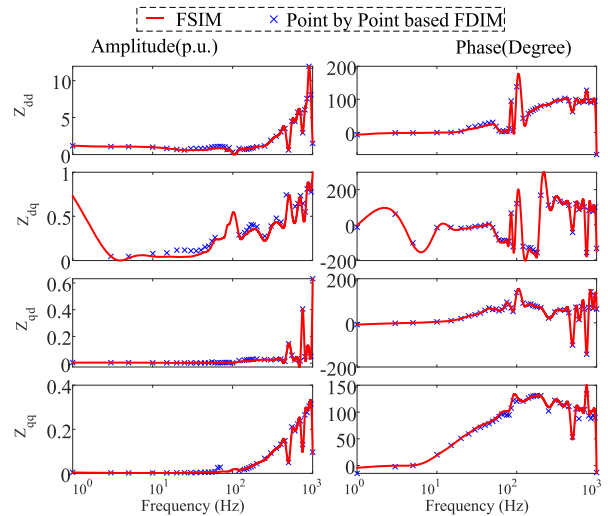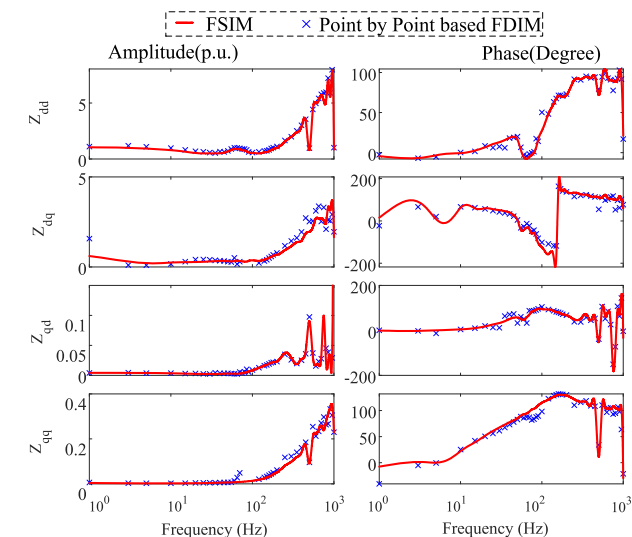The detailed comparison results of amplitude and phase response of these three sets of operating points are presented

FIGURE 13. Comparison of the amplitude and phase responses of the four impedance elements of the WTG1 for set 2 in Table 4.

in Figs. 12, 13, and 14, respectively. In these plots, the red solid line represents the impedance value from the measurement, and the blue cross point represents the point-by-point based FDIM. Although the prediction results for the point-by-point FDIM are not as perfect as the simulation results above, they still exhibit a sufficient accuracy. Now due to the high order of the IM, the curve-fitting based FDIM does not work.

VI. CONCLUSION

As is well-known, the impedance of a white-box device can be theoretically derived, but that of a black-box device can only be obtained from measurements. Until now the IM measurement is generally believed as a dominant workable method in electric power engineering. Since in the IM measurement, the impedance is highly correlated with operating points, it becomes difficult to quickly obtain impedances for a large number of operating points. Especially, as any impedance measurement is possible only for stable working conditions and the generalized Nyquist criterion can only be used when the impedance amplitude-frequency response is known, it is difficult to predict its small-signal stability before the VSC's connection to the grid, which might be either stable or unstable. All these might restrict the IM measurement application in many practical problems.

The main purpose of this paper is to solve this challenging problem for a fast impedance prediction under both the black-box and variable operating conditions, by relying on a completely decoupled parameter identification algorithm and several already-known impedance measurement data only. In particular, based on this IM prediction algorithm, the impedance becomes apparent immediately, on the basis of only 28 independent IM measurements. The fully-decoupled impedance prediction algorithm has been found accurate and efficient, and it has been widely verified by the simulations

TABLE 5. Comparison of different impedance methods.

Impedance methods	Properties	Advantages	Disadvantages
FSIM [12]–[15]	Black-box Experiment-driven	Simple, wide application Without systematic error	Experiment-dependent Unable to predict
ANN-based IE [24]	Black-box Data-driven	Data forecasting Simple	Lack of physical meanings Greatly influenced by training data With systematic error
MI-based IE [25]	Black-box Data-driven	Data forecasting Simple	Lack of physical meanings Values outside the interpolation interval are inaccurate With systematic error
GCPE [23]	Gray-box Model-driven	Data forecasting Without systematic error	Complicated Control structures must be known in advance
NDIM [26]	Gray-box Model-driven	Data forecasting Without systematic error	Complicated PLL-structure-dependent Neglecting the dynamics of the DC side
FDIM	Black-box Model-driven	Data forecasting Without systematic error Adaptive for various structures	Complicated Many calculation steps needed

and experiments. When the active power into the DC capacitor side is not constant in a more realistic environment, such as in the case of direct-drive wind turbines, it is found that the algorithm also works well. In addition, as the transfer function curve fitting algorithm, working as an auxiliary tool, is useful only when the order of the system is low, the original point-by-point based FDIM should be used in experiments.

Finally, to make the relation of our algorithm: FDIM, with all existing major IM methods in the literature clearer, a comparison is presented in Appendix E, with an accompanying Table 5. Therefore, the developed impedance prediction FDIM is expected to be capable of working as a supplemental technique of the IM measurement. It is useful for studies on relevant problems in various practical engineering environments, such as IM prediction for unknown operating conditions, stability boundary determination, and small-signal fault discrimination under a large amount of working conditions.

APPENDIX A
SMALL SIGNAL MODELING OF SYNCHRONIZATION CONTROL PARTS IN A UNIFIED FORM
A. PHASE LOCKING LOOP (PLL)
For the PLL synchronization in Fig. 1(b), recall that the PLL output angle in the small signal is

$$\Delta\theta = \Delta V_q^c \left(k_{p4} + k_{i4}/s\right)/s \qquad (37)$$

Substituting (37) into (5), we obtain

$$\Delta\theta = \frac{k_{p4} + k_{i4}/s}{s + V_d\left(k_{p4} + k_{i4}/s\right)} \Delta V_q^s \qquad (38)$$

and rewrite it in a unified form,

$$\Delta\theta = \begin{bmatrix} 0 & 0 \end{bmatrix} \begin{bmatrix} \Delta I_d^s \\ \Delta I_q^s \end{bmatrix} + \begin{bmatrix} 0 & \dfrac{G_{PLLn}}{G_{PLLd}} \end{bmatrix} \begin{bmatrix} \Delta V_d^s \\ \Delta V_q^s \end{bmatrix} \qquad (39)$$

where $G_{PLLn} = k_{p4} + k_{i4}/s$ and $G_{PLLd} = s + V_d\left(k_{p4} + k_{i4}/s\right)$.

B. POWER-SYNCHRONIZATION CONTROL OR BASIC DROOP CONTROL
For the power-synchronization control in Fig. 3(a) and the basic droop control in Fig. 3(b), their $\Delta\theta$'s are the same after the small-signal derivations. Namely,

$$\Delta\theta = \frac{-K_p}{s}\left(\begin{bmatrix} V_d & V_q \end{bmatrix} \begin{bmatrix} \Delta I_d^s \\ \Delta I_q^s \end{bmatrix} + \begin{bmatrix} I_d & I_q \end{bmatrix} \begin{bmatrix} \Delta V_d^s \\ \Delta V_q^s \end{bmatrix}\right) \qquad (40)$$

C. DROOP CONTROL WITH LOW-PASS FILTERS
Under the droop control with the low-pass filters in Fig. 3(c), we have

$$\Delta\theta = \frac{-K_p\omega_p}{s(s+\omega_p)}\left(\begin{bmatrix} V_d & V_q \end{bmatrix} \begin{bmatrix} \Delta I_d^s \\ \Delta I_q^s \end{bmatrix} + \begin{bmatrix} I_d & I_q \end{bmatrix} \begin{bmatrix} \Delta V_d^s \\ \Delta V_q^s \end{bmatrix}\right) \qquad (41)$$

D. VIRTUAL SYNCHRONOUS GENERATOR CONTROL
Under the virtual synchronous generator control in Fig. 3(d), we have

$$\Delta\theta = \frac{-\left(\begin{bmatrix} V_d & V_q \end{bmatrix} \begin{bmatrix} \Delta I_d^s \\ \Delta I_q^s \end{bmatrix} + \begin{bmatrix} I_d & I_q \end{bmatrix} \begin{bmatrix} \Delta V_d^s \\ \Delta V_q^s \end{bmatrix}\right)}{(Js + D_p)\omega_0 s} \qquad (42)$$
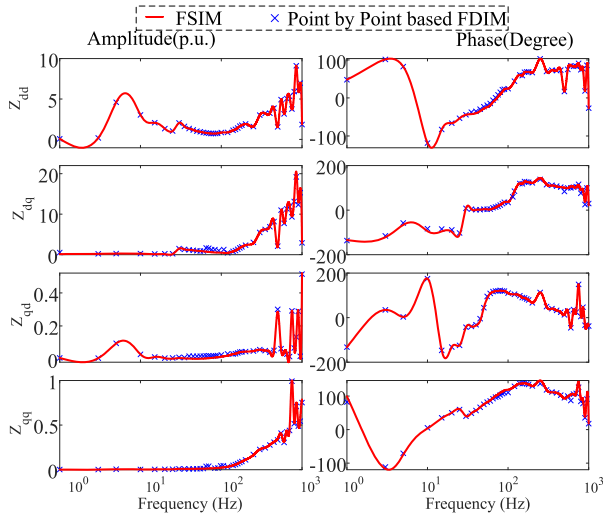
FIGURE 14. Comparison of the amplitude and phase responses of the four impedance elements of the WTG1 for set 3 in Table 4.

Therefore, for all these typical synchronization controls, we can have a general relation between the synchronization phase mismatch $\Delta\theta$ and the small-signal variables of terminal voltage and current, as shown in (7).

APPENDIX B
PROOF AND PRECONDITION OF EQUIVALENCE RELATION BETWEEN THE MODEL PARAMETER VECTORS AND THE SOLUTIONS OF EQUATIONS

Define vectors α and β

$$
\begin{cases}
\boldsymbol{\alpha} = \begin{bmatrix} b_1^T & b_2^T & a_1^T & a_2^T \end{bmatrix}^T \\
\boldsymbol{\beta} = \begin{bmatrix} b_3^T & b_4^T & a_3^T & a_4^T \end{bmatrix}^T
\end{cases} \quad (43)
$$

They can be expressed as $\boldsymbol{\alpha} = k_1\boldsymbol{\eta}_1 + k_2\boldsymbol{\eta}_2 + \cdots + k_n\boldsymbol{\eta}_n$ and $\boldsymbol{\beta} = k_1'\boldsymbol{\eta}_1 + k_2'\boldsymbol{\eta}_2 + \cdots + k_n'\boldsymbol{\eta}_n$, where k_i and k_i', $i = 1, 2, \ldots, n$ are constants and $\boldsymbol{\eta}_1, \boldsymbol{\eta}_2, \ldots, \boldsymbol{\eta}_n$ are the fundamental solutions of (27) and (28), they are linearly independent obviously.

Let $E_j = \begin{bmatrix} H_1^T & H_2^T & H_3^T & H_4^T \end{bmatrix}$, $j = 1, 2, 3, 4$, where $H_i = I_{10\times10}$ for $i = j$ and $H_i = 0_{10\times10}$ for $i \neq j$, $i = 1, 2, 3, 4$. Then we obtain

$$
\begin{cases}
b_1 = E_1\boldsymbol{\alpha}, \ b_2 = E_2\boldsymbol{\alpha}, \ a_1 = E_3\boldsymbol{\alpha}, \ a_2 = E_4\boldsymbol{\alpha}, \\
b_3 = E_1\boldsymbol{\beta}, \ b_4 = E_2\boldsymbol{\beta}, \ a_3 = E_3\boldsymbol{\beta}, \ a_4 = E_4\boldsymbol{\beta}.
\end{cases} \quad (44)
$$

Substituting (43) and (44) into (17) gives

$$
A_0 = b_1 b_4^T - b_2 b_3^T = E_1(\alpha\beta^T - \beta\alpha^T)E_2^T
$$
$$
= \sum_{i=1}^{n}\sum_{j=1}^{n}(k_i k_j' - k_j k_i')E_1(\eta_i\eta_j^T - \eta_j\eta_i^T)E_2^T
$$

$$
A_{11} = a_1 b_4^T - a_3 b_2^T = E_3(\alpha\beta^T - \beta\alpha^T)E_2^T
$$
$$
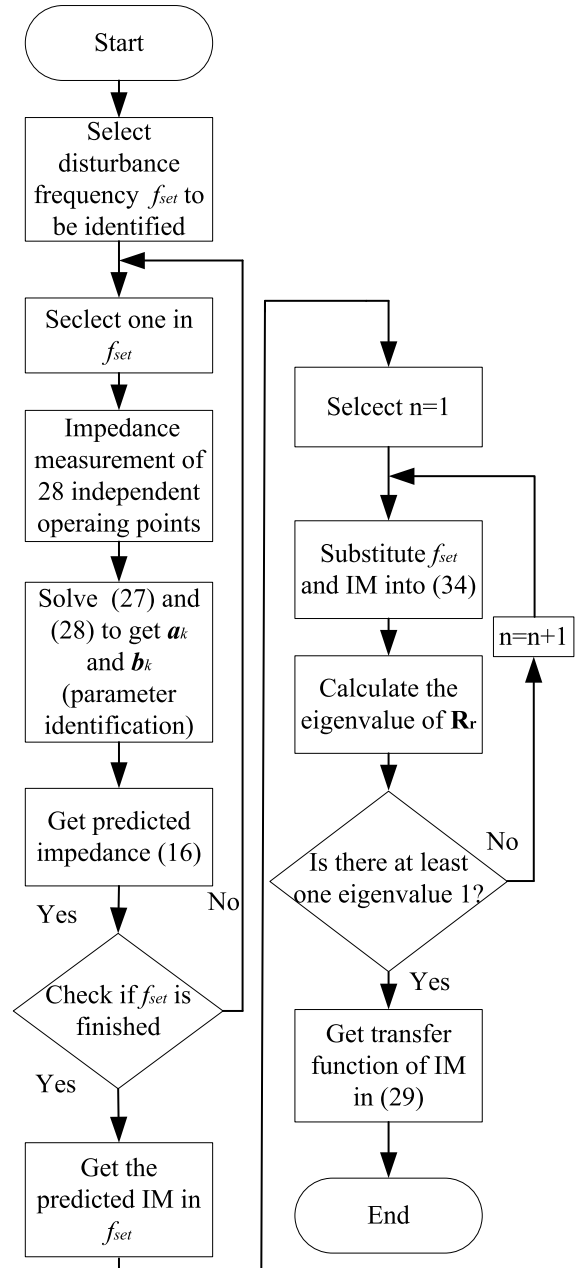= \sum_{i=1}^{n}\sum_{j=1}^{n}(k_i k_j' - k_j k_i')E_3(\eta_i\eta_j^T - \eta_j\eta_i^T)E_2^T
$$

FIGURE 15. Flow chart for the point-by-point based FDIM prediction algorithm, mainly consisting of the impedance prediction part (left) and the curve fitting part (right).

$$
A_{12} = a_2 b_4^T - a_4 b_2^T = E_4(\alpha\beta^T - \beta\alpha^T)E_2^T
$$
$$
= \sum_{i=1}^{n}\sum_{j=1}^{n}(k_i k_j' - k_j k_i')E_4(\eta_i\eta_j^T - \eta_j\eta_i^T)E_2^T
$$

$$
A_{21} = a_3 b_1^T - a_1 b_3^T = E_1(\alpha\beta^T - \beta\alpha^T)E_3^T
$$
$$
= \sum_{i=1}^{n}\sum_{j=1}^{n}(k_i k_j' - k_j k_i')E_1(\eta_i\eta_j^T - \eta_j\eta_i^T)E_3^T
$$

$$
A_{22} = a_4 b_1^T - a_2 b_3^T = E_1(\alpha\beta^T - \beta\alpha^T)E_4^T
$$

$$= \sum_{i=1}^{n} \sum_{j=1}^{n} (k_i k_j' - k_j k_i') E_1 (\eta_i \eta_j^T - \eta_j \eta_i^T) E_4^T \quad (45)$$

Take the calculation of Z_{dd} as an example. After substituting (45) into (16), we have

$$
\begin{aligned}
Z_{dd} &= \frac{x^T A_{11} x}{x^T A_0 x} \\
&= \frac{\sum_{i=1}^{n} \sum_{j=1}^{n} (k_i k_j' - k_j k_i') x^T E_3 (\eta_i \eta_j^T - \eta_j \eta_i^T) E_2^T x}{\sum_{i=1}^{n} \sum_{j=1}^{n} (k_i k_j' - k_j k_i') x^T E_1 (\eta_i \eta_j^T - \eta_j \eta_i^T) E_2^T x}
\end{aligned} \quad (46)
$$

To make Z_{dd} independent of the coefficients $k_1, k_2, \ldots, k_n$ and $k_1', k_2', \ldots, k_n'$, only when $\frac{x^T E_3 (\eta_i \eta_j^T - \eta_j \eta_i^T) E_2^T x}{x^T E_1 (\eta_i \eta_j^T - \eta_j \eta_i^T) E_2^T x}$ is equal in any value of i and j, then $Z_{dd} = \frac{x^T E_3 (\eta_i \eta_j^T - \eta_j \eta_i^T) E_2^T x}{x^T E_1 (\eta_i \eta_j^T - \eta_j \eta_i^T) E_2^T x}$, for $i, j = 1, 2, \ldots, n$.

Then, the precondition is that for $\eta_1, \eta_2, \ldots, \eta_n$, any two of the solutions as α and β are substituted into the Z_{dd} calculated by (22) and (21) are equal.

APPENDIX C

The expressions of K_1, K_2, H_1, and H_2 in (32) are as follows:

$$K_1 = \begin{bmatrix} 1 & s_0 & \cdots & s_0^n \\ 1 & s_1 & \cdots & s_1^n \\ \vdots & \vdots & \ddots & \vdots \\ 1 & s_n & \cdots & s_n^n \end{bmatrix} \quad (47)$$

$$K_2 = \begin{bmatrix} 1 & s_{n+1} & \cdots & s_{n+1}^n \\ 1 & s_{n+2} & \cdots & s_{n+2}^n \\ \vdots & \vdots & \ddots & \vdots \\ 1 & s_{2n+1} & \cdots & s_{2n+1}^n \end{bmatrix} \quad (48)$$

$$H_1 = \begin{bmatrix} f_{(s_0)} \cdot 1 & f_{(s_0)} \cdot s_0 & \cdots & f_{(s_0)} \cdot s_0^n \\ f_{(s_1)} \cdot 1 & f_{(s_1)} \cdot s_1 & \cdots & f_{(s_1)} \cdot s_1^n \\ \vdots & \vdots & \ddots & \vdots \\ f_{(s_n)} \cdot 1 & f_{(s_n)} \cdot s_n & \cdots & f_{(s_n)} \cdot s_n^n \end{bmatrix} \quad (49)$$

$$H_2 = \begin{bmatrix} f_{(s_{n+1})} \cdot 1 & f_{(s_{n+1})} \cdot s_{n+1} & \cdots & f_{(s_{n+1})} \cdot s_{n+1}^n \\ f_{(s_{n+2})} \cdot 1 & f_{(s_{n+2})} \cdot s_{n+2} & \cdots & f_{(s_{n+2})} \cdot s_{n+2}^n \\ \vdots & \vdots & \ddots & \vdots \\ f_{(s_{2n+1})} \cdot 1 & f_{(s_{2n+1})} \cdot s_{2n+1} & \cdots & f_{(s_{2n+1})} \cdot s_{2n+1}^n \end{bmatrix} \quad (50)$$

APPENDIX D
FLOW CHART FOR THE FDIM

A flow chart for illustrating the major steps of the point-by-point based FDIM is shown in Fig. 15.

APPENDIX E
COMPARISON OF DIFFERENT IMPEDANCE ACQUISITION METHODS

In order to make the properties of FDIM clearer, the advantages and disadvantages with five other major impedance identification methods are presented in Tab. 5, including the FSIM, artificial neural network-based impedance estimation (ANN-based IE) [24], multidimensional interpolation based impedance estimation method (MI-based IE) [25] gray-box-based controller parameter estimation (GCPE) [23], and the nearly decoupled impedance model (NDIM) [26]. The FSIM is one of experiment-driven and black-box impedance measurement methods without systematic error. It is simple and accurate. What is more, it has wide and mature applications in engineering practice. However, it cannot be used to predict impedance values. The ANN-based IE is one of data-driven and black-box impedance prediction methods with systematic error, but it lacks physical meanings and is often greatly influenced by the training data. The MI-based IE is one of data-driven and black-box impedance prediction methods with systematic error as ANN-based IE. It also lacks physical meanings and the predicted values outside the interpolation interval are inaccurate. The GCPE is one of model-driven and gray-box impedance identification methods without systematic error, but the control structures must be known in advance. The NDIM is one of model-driven and black-box impedance prediction methods without systematic error. However, it is valid under the PLL synchronization control structure, with the dynamic behaviors of the DC side completely neglected. In contrast, the proposed FDIM in this paper is a model-driven and black-box impedance method without systematic error. As we have seen, besides the VSC and VSG, it is also valid for wind turbines and other control structures. Hence it is unique for electric power engineering applications.

REFERENCES

[1] J. A. Turner, "A realizable renewable energy future," *Science*, vol. 285, no. 5428, pp. 687–689, 1999.

[2] F. Blaabjerg and K. Ma, "Future on power electronics for wind turbine systems," *IEEE J. Emerg. Sel. Topics Power Electron.*, vol. 1, no. 3, pp. 139–152, Sep. 2013.

[3] X. Wang and F. Blaabjerg, "Harmonic stability in power electronic-based power systems: Concept, modeling, and analysis," *IEEE Trans. Smart Grid*, vol. 10, no. 3, pp. 2858–2870, May 2019.

[4] X. Yuan, J. Hu, and S. Cheng, "Multi-time scale dynamics in power electronics-dominated power systems," *Frontiers Mech. Eng.*, vol. 12, no. 3, pp. 303–311, Sep. 2017.

[5] Y. Ji, W. He, S. Cheng, J. Kurths, and M. Zhan, "Dynamic network characteristics of power-electronics-based power systems," *Sci. Rep.*, vol. 10, no. 1, pp. 1–16, Dec. 2020.

[6] R. Ma, Z. Yang, S. Cheng, and M. Zhan, "Sustained oscillations and bifurcations in three-phase voltage source converter tied to AC grid," *IET Renew. Power Gener.*, vol. 14, no. 18, pp. 3770–3781, 2020.

[7] Z. Yang, R. Ma, S. Cheng, and M. Zhan, "Nonlinear modeling and analysis of grid-connected voltage-source converters under voltage dips," *IEEE J. Emerg. Sel. Topics Power Electron.*, vol. 8, no. 4, pp. 3281–3292, Dec. 2020.

[8] Z. Yang, J. Yu, J. Kurths, and M. Zhan, "Nonlinear modeling of multi-converter systems within DC-link timescale," *IEEE J. Emerg. Sel. Topics Circuits Syst.*, vol. 11, no. 1, pp. 5–16, Mar. 2021.

[9] G. O. Kalcon, G. P. Adam, O. Anaya-Lara, S. Lo, and K. Uhlen, "Small-signal stability analysis of multi-terminal VSC-based DC transmission systems," *IEEE Trans. Power Syst.*, vol. 27, no. 4, pp. 1818–1830, Nov. 2012.

[10] M. K. Zadeh, M. Amin, J. A. Suul, M. Molinas, and O. B. Fosso, "Small-signal stability study of the Cigré DC grid test system with analysis of participation factors and parameter sensitivity of oscillatory modes," in *Proc. Power Syst. Comput. Conf.*, Aug. 2014, pp. 1–8.

[11] J. Yu, Z. Yang, J. Kurths, and M. Zhan, "Small-signal stability of multi-converter infeed power grids with symmetry," *Symmetry*, vol. 13, no. 2, p. 157, Jan. 2021.

[12] V. Valdivia, A. Lázaro, A. Barrado, P. Zumel, C. Fernández, and M. Sanz, "Impedance identification procedure of three-phase balanced voltage source inverters based on transient response measurements," *IEEE Trans. Power Electron.*, vol. 26, no. 12, pp. 3810–3816, Dec. 2011.

[13] M. Cespedes and J. Sun, "Three-phase impedance measurement for system stability analysis," in *Proc. IEEE 14th Workshop Control Modeling Power Electron. (COMPEL)*, Jun. 2013, pp. 1–6.

[14] G. Francis, R. Burgos, D. Boroyevich, F. Wang, and K. Karimi, "An algorithm and implementation system for measuring impedance in the D-Q domain," in *Proc. IEEE Energy Convers. Congr. Expo.*, Sep. 2011, pp. 3221–3228.

[15] J. Fang, H. Deng, and S. M. Goetz, "Grid impedance estimation through grid-forming power converters," *IEEE Trans. Power Electron.*, vol. 36, no. 2, pp. 2094–2104, Feb. 2021.

[16] L. Harnefors, M. Bongiorno, and S. Lundberg, "Input-admittance calculation and shaping for controlled voltage-source converters," *IEEE Trans. Ind. Electron.*, vol. 54, no. 6, pp. 3323–3334, Dec. 2007.

[17] M. Cespedes and J. Sun, "Impedance modeling and analysis of grid-connected voltage-source converters," *IEEE Trans. Power Electron.*, vol. 29, no. 3, pp. 1254–1261, Mar. 2014.

[18] B. Wen, D. Boroyevich, R. Burgos, P. Mattavelli, and Z. Shen, "Analysis of D-Q small-signal impedance of grid-tied inverters," *IEEE Trans. Power Electron.*, vol. 31, no. 1, pp. 675–687, Jan. 2016.

[19] J. Liu, X. Du, Y. Shi, and H.-M. Tai, "Impedance measurement of three-phase inverter in the stationary frame using frequency response analyzer," *IEEE Trans. Power Electron.*, vol. 35, no. 9, pp. 9390–9401, Sep. 2020.

[20] Y. Yan, X. Yuan, and J. Hu, "Stationary-frame modeling of VSC based on current-balancing driven internal voltage motion for current control timescale dynamic analysis," *Energies*, vol. 11, no. 2, p. 374, Feb. 2018.

[21] M. Amin and M. Molinas, "Small-signal stability assessment of power electronics based power systems: A discussion of impedance- and eigenvalue-based methods," *IEEE Trans. Ind. Appl.*, vol. 53, no. 5, pp. 5014–5030, Sep./Oct. 2017.

[22] Z. Yang, C. Mei, S. Cheng, and M. Zhan, "Comparison of impedance model and amplitude–phase model for power-electronics-based power system," *IEEE J. Emerg. Sel. Topics Power Electron.*, vol. 8, no. 3, pp. 2546–2558, Sep. 2020.

[23] M. Amin and M. Molinas, "A gray-box method for stability and controller parameter estimation in HVDC-connected wind farms based on nonparametric impedance," *IEEE Trans. Ind. Electron.*, vol. 66, no. 3, pp. 1872–1882, Mar. 2019.

[24] M. Zhang, X. Wang, D. Yang, and M. G. Christensen, "Artificial neural network based identification of multi-operating-point impedance model," *IEEE Trans. Power Electron.*, vol. 36, no. 2, pp. 1231–1235, Feb. 2021.

[25] H. Gong, X. Wang, and D. Yang, "DQ-frame admittance estimation of three-phase converters with a wide range of operating points," *TechRxiv*, pp. 1–9, Mar. 2021, doi: 10.36227/techrxiv.14229071.v1.

[26] W. Liu, X. Xie, J. Shair, and X. Li, "A nearly decoupled admittance model for grid-tied VSCs under variable operating conditions," *IEEE Trans. Power Electron.*, vol. 35, no. 9, pp. 9380–9389, Sep. 2020.

[27] W. Liu, X. Xie, J. Shair, H. Liu, and J. He, "Frequency-coupled impedance model-based sub-synchronous interaction analysis for direct-drive wind turbines connected to a weak AC grid," *IET Renew. Power Gener.*, vol. 13, no. 16, pp. 2966–2976, 2019.

[28] U. Markovic, O. Stanojev, P. Aristidou, and G. Hug, "Partial grid forming concept for 100% inverter-based transmission systems," in *Proc. IEEE Power Energy Soc. Gen. Meeting (PESGM)*, Aug. 2018, pp. 1–5.

[29] D. Pan, X. Wang, F. Liu, and R. Shi, "Transient stability of voltage-source converters with grid-forming control: A design-oriented study," *IEEE J. Emerg. Sel. Topics Power Electron.*, vol. 8, no. 2, pp. 1019–1033, Jun. 2020.

[30] B. Gustavsen and A. Semlyen, "Simulation of transmission line transients using vector fitting and modal decomposition," *IEEE Trans. Power Del.*, vol. 13, no. 2, pp. 605–614, Apr. 1998.

[31] B. Gustavsen and A. Semlyen, "Rational approximation of frequency domain responses by vector fitting," *IEEE Trans. Power Del.*, vol. 14, no. 3, pp. 1052–1061, Jul. 1999.

[32] K. De Brabandere, B. Bolsens, J. Van den Keybus, A. Woyte, J. Driesen, and R. Belmans, "A voltage and frequency droop control method for parallel inverters," *IEEE Trans. Power Electron.*, vol. 22, no. 4, pp. 1107–1115, Jul. 2007.

[33] L. Huang, H. Xin, Z. Wang, L. Zhang, K. Wu, and J. Hu, "Transient stability analysis and control design of droop-controlled voltage source converters considering current limitation," *IEEE Trans. Smart Grid*, vol. 10, no. 1, pp. 578–591, Jan. 2019.

[34] J. Alipoor, Y. Miura, and T. Ise, "Power system stabilization using virtual synchronous generator with alternating moment of inertia," *IEEE J. Emerg. Sel. Topics Power Electron.*, vol. 3, no. 2, pp. 451–458, Jun. 2015.

[35] Q.-C. Zhong, P.-L. Nguyen, Z. Ma, and W. Sheng, "Self-synchronized synchronverters: Inverters without a dedicated synchronization unit," *IEEE Trans. Power Electron.*, vol. 29, no. 2, pp. 617–630, Feb. 2014.

[36] C. Hu, K. Chen, S. Luo, B. Zhou, and L. Ding, "Small signal modeling and stability analysis of virtual synchronous generators," in *Proc. 20th Int. Conf. Electr. Mach. Syst. (ICEMS)*, Aug. 2017, pp. 1–5.

QI QIU was born in Fuzhou, Jiangxi, China, in 1997. He received the B.S. degree from North China Electronic Power University, Baoding, China, in 2018, and the M.Eng. degree in electrical engineer from the State Key Laboratory of Advanced Electromagnetic Engineering and Technology, School of Electrical and Electronic Engineering, Huazhong University of Science and Technology, in 2021.

He is currently with State Grid Nanchang Electric Power Supply Company. His research interests include stability and control of power systems with renewable energy generation, such as impedance model, harmonic linearization, and small-signal stability analysis.

YIFAN HUANG was born in Fuzhou, Jiangxi, China, in 1997. He received the B.S. degree from North China Electronic Power University, Baoding, China, in 2019. He is currently pursuing the M.Eng. degree in electrical engineering with the State Key Laboratory of Advanced Electronic Engineering, Huazhong University of Science and Technology.

His research interests include the ways to analyze the stability of power system with renewable energy generation, and in particular impedance modeling and analysis of the voltage-source converter, and stability and control of power systems with renewable energy generation, such as impedance model, harmonic linearization, and small-signal stability analysis.

RUI MA received the B.S. degree in electrical engineering from North China Electronic Power University, Baoding, China, in 2018. He is currently pursuing the Ph.D. degree in electrical engineering with the State Key Laboratory of Advanced Electromagnetic Engineering and Technology, School of Electrical and Electronic Engineering, Huazhong University of Science and Technology, Wuhan, China.

His research interests include the stability and control of renewable energy dominated power systems, such as wide bandwidth oscillation and transient stability analysis.

JÜRGEN KURTHS received the Ph.D. degree from the GDR Academy of Sciences, Berlin, Germany, in 1983.

From 1994 to 2008, he was a Full Professor with the University of Potsdam, Potsdam, Germany. Since 2008, he has been a Professor of nonlinear dynamics with the Humboldt University of Berlin, Berlin, and the Chair of the Research Domain Transdisciplinary Concepts, Potsdam Institute for Climate Impact Research, Potsdam. He has authored or coauthored more than 600 articles that are cited more than 42 000 times (H-index: 91). His current research interests include synchronization, complex networks, and time-series analysis and their applications. He became a member of the Academy of Europe in 2010, conferred eight honorary doctorates. He was a recipient of the Richardson Award of the European Geophysical Union in 2013. He is the Editor-in-Chief of *CHAOS*. He is a Highly Cited Researcher in engineering and physics.

MENG ZHAN (Member, IEEE) was born in Jingdezhen, Jiangxi, China, in 1974. He received the B.S. degree in physics and the Ph.D. degree in nonlinear physics from Beijing Normal University, Beijing, China, in 1996 and 2001, respectively.

He was a Postdoctoral Researcher with the National University of Singapore, Singapore, and the University of Toronto, Canada, from 2001 to 2006. He worked as a Full Professor with the Wuhan Institute of Physics and Mathematics, and the Chinese Academy of Sciences, from 2006 to 2015. In 2015, he joined the State Key Laboratory of Advanced Electromagnetic Engineering and Technology, School of Electrical and Electronic Engineering, Huazhong University of Science and Technology. He has long been engaged in the study of nonlinear dynamics theory of complex systems in multiple directions, such as coupled nonlinear systems, chaos synchronization and control, pattern formation, and complex network dynamics. He has published more than 100 SCI articles in internationally peer-reviewed journals. His current research interests include renewable energy integration stability, power-electronic-based power system dynamics, and nonlinear analysis of power systems.

● ● ●